Smart Structures and Systems, *Vol. 16, No. 3 (2015) 555-577*
DOI: http://dx.doi.org/10.12989/sss.2015.16.3.555

A SMA-based morphing flap: conceptual and advanced design

Salvatore Ameduri*[1], Antonio Concilio[1a] and Rosario Pecora[2b]

[1]Smart Structures and Materials Lab., Centro Italiano Ricerche Aerospaziali, Via Maiorise, 81043, Capua (CE), Italy
[2]Department of Aerospace Engineering, Università degli Studi di Napoli "Federico II", Via Claudio, 21, 80125, Napoli, Italy

(Received March 30, 2014, Revised December 20, 2014, Accepted March 28, 2015)

Abstract. In the work at hand, the development of a morphing flap, actuated through shape memory alloy load bearing elements, is described. Moving from aerodynamic specifications, prescribing the morphed shape enhancing the aerodynamic efficiency of the flap, a suitable actuation architecture was identified, able to affect the curvature. Each rib of the flap was split into three elastic elements, namely "cells", connected each others in serial way and providing the bending stiffness to the structure. The edges of each cell are linked to SMA elements, whose contraction induces rotation onto the cell itself with an increase of the local curvature of the flap airfoil. The cells are made of two metallic plates crossing each others to form a characteristic "X" configuration; a good flexibility and an acceptable stress concentration level was obtained non connecting the plates onto the crossing zone. After identifying the main design parameters of the structure (i.e. plates relative angle, thickness and depth, SMA length, cross section and connections to the cell) an optimization was performed, with the scope of enhancing the achievable rotation of the cell, its ability in absorbing the external aerodynamic loads and, at the same time, containing the stress level and the weight. The conceptual scheme of the architecture was then reinterpreted in view of a practical realization of the prototype. Implementation issues (SMA - cells connection and cells relative rotation to compensate the impressed inflection assuring the SMA pre-load) were considered. Through a detailed FE model the prototype morphing performance were investigated in presence of the most severe load conditions.

Keywords: shape memory alloys; smart structures; morphing; flap

1. Introduction

Adaptive modifications, morphing, of aerodynamic surfaces offer the possibility of strongly enhancing aircraft performance and widely enlarging the entire flight envelope, as widely reported in literature, as for instance, (Stanewsky 2001, Lesieutre 2011).

The potential benefits in terms of aerodynamic efficiency (drag reduction, L/D ratio increase, manoeuvrability or stability levels - commands effectiveness, time response, etc.), environmental

*Corresponding author, Ph.D., E-mail: s.ameduri@cira.it
[a] Ph.D., E-mail: a.concilio@cira.it
[b] Ph.D., E-mail: rosario.pecora@unina.it

http://www.techno-press.org/?journal=sss&subpage=8 ISSN: 1738-1584 (Print), 1738-1991 (Online)

impact ratio (reduction of general emissions level, see for instance as reference what reported in the ACARE agenda, website 2012), maintenance easiness (parts number reduction, simpler architectures, etc.), weight and cost reduction and many others, largely justify the increasing interest of the research community within this specific field.

The advent of novel technologies, as the ones based on the implementation of Shape Memory Alloys (SMA) based actuators, gave a further boost to the research in the adaptive structural systems. The availability of very compact elements, able to produce extremely large point forces, allowed in fact thinking of new design solutions, considered at those times impossible with standard technologies. The evolution of the morphing concept led indeed to other surprises, but this story is out of the scope of this paper, (SARISTU Project website). Anyway, the immediate result has been the availability of a large quantity of original applications, characterised by high technology readiness levels and addressed to different aircraft types (fixed and rotary wings; civil and military, small and large size, spanning from UAV to civil freighter).

Bibliography is rich of many and many works, facing the many aspects of morphing, ranging from materials and components enablers, (Mcknight *et al.* 2010, Olympio and Gandhi 2010), the development of suitable architectures for high-strain transmission, (Maheri and Isikveren 2011), the assessment of appropriate wing deployable frames (Zhao *et al.* 2012), bio-morph investigations and design oriented schemes moving from the aerodynamics of real birds, (Carruthers *et al.* 2010), design and modelling of SMA actuators, integrated within structural elements, (Concilio and Ameduri 2013), and many others. Many authors did arrive to large-scale demonstrators as in the case of the all-composite flexible flap, (Wildschek *et al.* 2010), the adaptive wing tip, (Daniele *et al.* 2012), and so on. Also, peculiar control and activation techniques have been developed as the partial activation of shape memory components, (Langbein and Welp 2009) or fitted control strategies suited for conventional and innovative actuators, (Dimino and Concilio 2013, Grigorie *et al.* 2011a, b). Reported references are just few examples among the very large mass of publications that is available in the world-wide scientific scenario.

In the current work, the conceptual design and the preliminary assessment of a single slotted flap is presented, actuated by SMA-based actuators. Both the envisaged architecture and the design procedure are original contributions to the research on the addressed topics and refer to realistic distributions of aerodynamic and structural loads, developed in operative conditions. Namely, the geometry (target envelope shapes) and load specifications were issued within the Clean Sky Joint Technology Initiative (JTI) and faced is some other jobs from the same authors, (Pecora *et al.* 2013, Ameduri *et al.* 2013).

The architecture is basically derived by splitting the flap ribs into segmented components, joined through concentrated elastic elements. The lower edges of these components are connected by SMA 1D elements, with the twofold aim of cooperating to absorb external loads and commanding downwards deflections. A specific design procedure is presented, taking into account both the cell geometrical non-linearity and the characteristic SMA features (recoverable strain vs structural rigidity; activation level vs temperature). The scheme is implemented into a genetic algorithm in order to find the optimal project solution in terms of system weight and needed power supply, constrained by the materials limitation. Geometrical constraints (volume and general dimensions) are instead considered in the preliminary layout definition and are “a priori” satisfied.

After setting the cell parameters, the advanced design of the entire flap is dealt with. Suitable solutions are provided to practical manufacture aspects as the SMA system electrical insulation (the active elements strain recovery is driven by heating, generated by an inner electrical current – Joule effect) and the cell pre-load. A FE model of the entire flap is finally realised. Static analyses

prove the flap ability in producing the desired shape variation (morphing) while withstanding the external aerodynamic loads. The study, completed by instability and normal mode investigations, gives an exhaustive prediction of the flap behaviour and its application limits.

2. Aerodynamic issues

The reference device is a single slotted flap, able to translate back- and down-ward when rotating clockwise (lift enhancer). Adaptive camber variations are supposed to increase the hyper-lift generation performance while leaving unaffected the basic kinematic system. A schematic of the airfoil integrated with the morphing-enhanced flap is qualitatively illustrated in Fig. 1.

Aerodynamic investigations led to the target morphed geometry presented in Fig. 2, left, assuring the specified hyperlift. According to the design specifications, the fore flap segment (up to 20% Mean Aerodynamic Chord, MAC, red domain) was constrained to be rigid, in order to allow hosting the attachment to the deploying kinematic system.

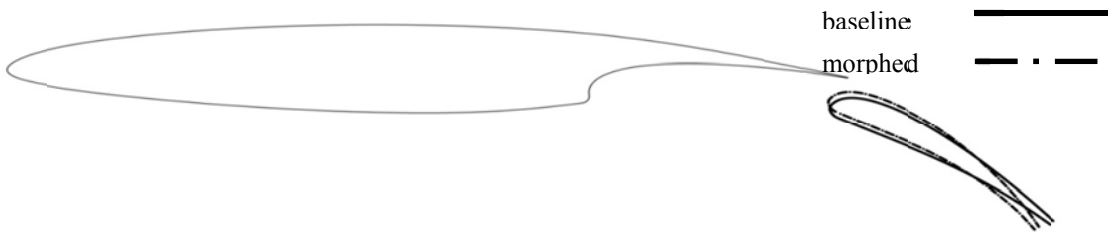

Fig. 1 Airfoil with the deployed flap in morphed (dashed) and unmorphed (solid) configuration

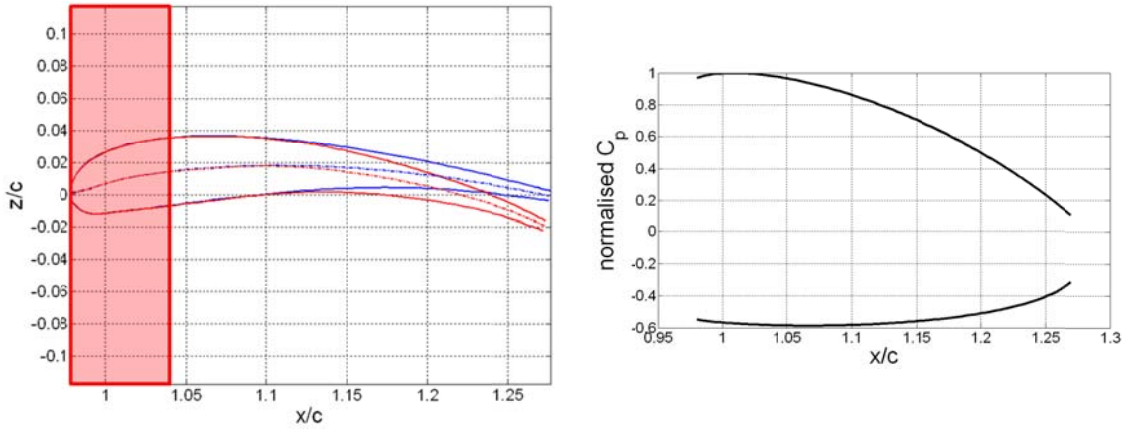

Fig. 2 Left: Clean and morphed flap shapes (z/c; x/c); right: pressure distribution

The remaining part of the device was instead optimized for landing and take-off conditions (red line) while maintaining the original shape when retracted (blue line), Fig. 2. The morphing system is then aimed at assuring the achievement of the specified shape under the action of the external aerodynamic and structural loads while preserving structural integrity. In this work, the most severe considered load condition is achieved at sea level (p = 1 atm, T = 20°C), at a landing speed of 180 Km/h.

3. Selected morphing strategy

The morphing system has to meet the following specs.:

1. fit the prescribed shape under the reference loads;
2. exhibit structural integrity and stability;
3. keep low weight and electrical power needs.

A compromise between the first two aspects is antithetical. The structure should in fact be quite flexible to attain the target shape but rigid enough to sustain inner and outer external loads. A structure with concentrated elastic elements and therein reinforced and actuated by load-bearing actuators can represent a suitable answer to the abovementioned paradox. Shape Memory Alloys (SMA) based devices seem to be a good candidate among the different typologies of applicable systems. This kind of material can indeed transmit large forces and deformations, exhibit adequate strength capabilities and offer the possibility of being integrated within limited room. Slow activation times, typical of thermal actuators, are compatible with the typical response of standard flaps (30 sec deployment time). While the necessity of adequately fitting the target shape would require an ideally infinite actuators and related degrees of freedom, this figure has to be naturally contained to a small number to avoid too complicate and heavy structures, leading in turn to high maintenance costs.

The selected architecture (Fig. 4, left) is made of segmented rib elements, serially connected through elastic metallic components (cells). Each cell is formed of two clamped-clamped crossing plates (making an "X") not interfering on the middle. This peculiar configuration guarantees a distributed bending flexibility, being the rotational pivot practically spread along the extension of the cell itself. A wide stress distribution follows, with consequent benefits in terms of fatigue life and achievable deflections. Cell bottom edges were hinged to SMA elements, contributing to the overall system rigidity and able to induce bending when activated.

Three cells per rib were considered, a configuration classically reported in bibliography (Nadar *et al.* 2013). Such layout is easily integrable within the limited available volumes and is herein demonstrated to allow a good level of approximation with respect to the target shape. Span-wise, a three-bay, 1 m homogeneous system is referred to; the ribs are connected through a number of spars, bolted at each cell front and back boundaries. Segmented upper and lower skins are riveted onto the spars and the rib parts. Non-structural, non actuated intermediate ribs (shape ribs) may be added to increase the skin performance at level of exhibited vertical deflection. The resulting system is then an articulated configuration with smooth edges at each of the blocks, for safety and aerodynamic reasons. The blowing flow among the segments, reduces lift performance but guarantees a lower drag.

4. Conceptual design and optimization

A dedicated procedure was set up for preliminarily sizing the three cells of each rib. The process is schematized in Fig. 3, left, as a block diagram. First of all, a basic configuration is assumed, in terms of: elastic plates length, thickness distribution and relative angle, SMA length and cross section dimensions, position of the shape memory alloy linear actuator with respect to the cell. The characteristic curve relating the force, generated by the SMA device, with the produced displacement along the force line, is computed through a FE model of the single X cell. This task is carried out by simply assigning a virtual negative thermal coefficient, α_T, to the SMA material and applying stepped thermal loads, T. The force, transmitted by the actuator to the structure, FSMA, is then obtained through the classical relation

$$F_{SMA} = E_{SMA} A_{SMA} (\varepsilon - \alpha_T T) \tag{1}$$

being E_{SMA} a virtual Young modulus assigned to the SMA material, A_{SMA} the SMA element cross section and ε the resulting deformation from the FE analysis. F_{SMA} is related to the component of the attained displacement onto the force line. A buckling analysis allows calculating the minimum force causing instability in the device, that is the upper limit to the actuation.

The system working excursion is then defined, by identifying the two extreme configurations, moving from the pre-load condition (i.e., the pre-stressed cell state, able to ensure the complete recovery after operation, indicated by $_{pl}$) to the full-deployed configuration (i.e., the cell maximum deflection, following a complete SMA activation, indicated by $_{wk}$). These points are individuated by crossing the cell force-displacement characteristic elastic curve with the martensite and austenite linear characteristics of the SMA that envelop its constitutive relation, Fig. 3, right (Concilio and Ameduri 2013). The elastic element line has a negative slope because its action is against the SMA movement.

If the force, produced by the shape memory alloy device in the full-activated condition, is under the buckling limits and the consequent stress level is within the material physical boundaries, the cell ability in bearing the external loads while keeping the attained deformed shape, is investigated. According to an established discretisation, the aerodynamic forces and moments are applied to the structural system, deriving its upward deflection. A schematic representation of the generic cell is reported in Fig. 4 while the possible values for each parameter are reported in Table 4. Four active ribs per meter span were considered. A genetic algorithm is then implemented to identify the optimal architecture in terms of:

- vertical coordinates of the elastic plates edges (points A, B C and D in Fig. 4); abscissas were in fact kept constant and assumed coincident with the vertical boundaries of the cells, Fig. 4 (maximum horizontal extension);
- plates thickness and width, having assumed a linear distribution of these parameters over the length;
- SMA hinges location inside each cell (points E and F in Fig. 4) and SMA cross section;
- Cell material, chosen among aluminium 7075-T6, stainless steel and titanium.

The optimization process targets to maximize the cell deflection, within stability and material limits (Tomassetti *et al.* 2011). The method allows finding configurations well exceeding required deflections, confirming its effectiveness and the potentiality of the investigated architecture. The genetic algorithm works on populations of 300 individuals for each cell, repeating the process twenty times.

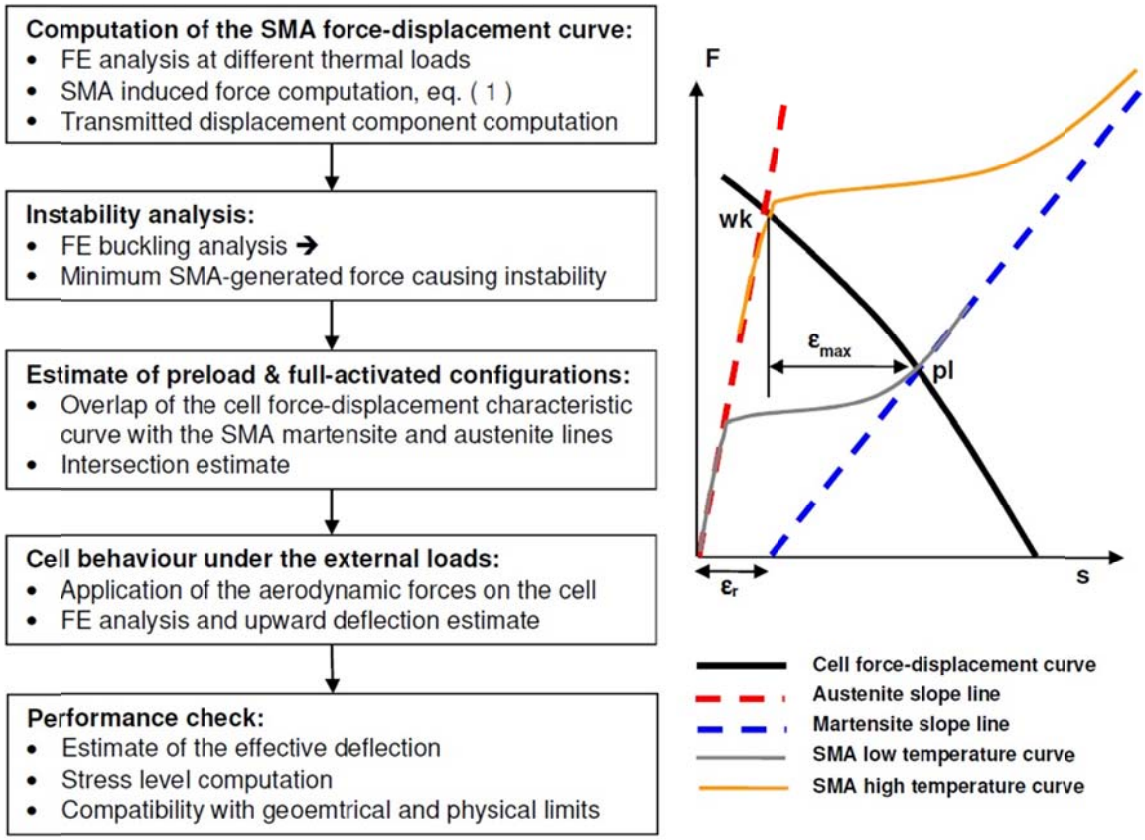

Fig. 3 Flowchart of the conceptual design (left); force-displacement representation of the cell (right)

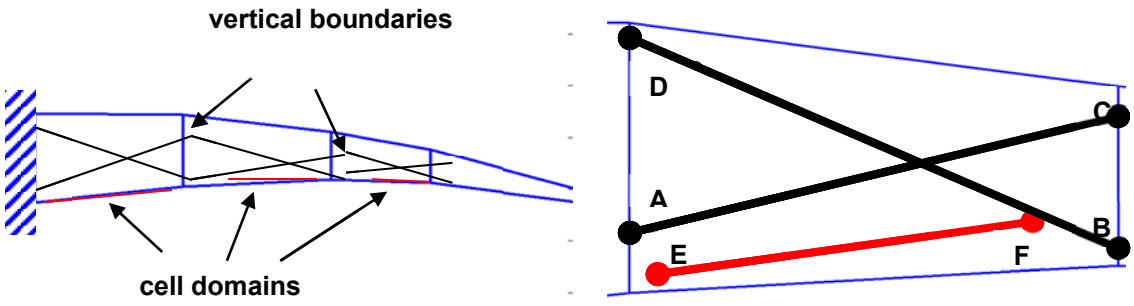

Fig. 4 Cells domains (left), schematic of a cell (right)

Table 1 Design parameters and variation ranges for the three cells

Design parameter	Range – Allowed Values		
	Cell 1	**Cell 2**	**Cell 3**
A, ordinate (mm)	-13.2 ÷ 0.00	1.60 ÷ 13.3	9.0 ÷ 2.40
B, ordinate (mm)	1.60 ÷ 12.6	8.70 ÷ 15.7	5.40 ÷ 13.4
C, ordinate (mm)	6.24 ÷ 7.20	4.48 ÷ 5.55	28.8 ÷ 37.6
D, ordinate (mm)	5.70 ÷ 7.30	5.48 ÷ 7.20	40.1 ÷ 54.1
E, abscissa (mm)	140.5 ÷ 180.5	270.0 ÷ 324.0	399.0 ÷ 418.1
E, ordinate (mm)	-13.2 ÷ 5.20	1.60 ÷ 16.1	9.10 ÷ 16.2
F, abscissa (mm)	23.3 ÷ 27.0	352.0 ÷ 399.0	464.5 ÷ 485.6
F, ordinate (mm)	10.1 ÷ 1.60	15.1 ÷ 17.6	4.90 ÷ 13.4
Plate thickness (mm)*	1.00 ÷ 10.0	1.00 ÷ 15.0	0.50 ÷ 5.0
Plate width (mm)*	10.0 ÷ 120.0	10.0 ÷ 100.0	1.0 ÷ 50.0
SMA cross section (mm^2)	10.0 ÷ 300.0	10.0 ÷ 240.0	10.0 ÷ 180.0
Cell possible materials	Stainless steel; Aluminium alloy; Titanium alloy		
Aerodynamic force resultant (N)	855.9	552.6	287.7
Aerodynamic moment resultant (Nm)	278.3	131.4	43.9

* initial & final values are searched for; a linear variation of the thickness and width is assumed, along the plate length

The individual performance drives the following selection and the further generation of a new set of solutions, according to the standard rules of this kind of algorithms, paying specific attention at avoiding the occurrence of premature convergence (screening, choice, crossover, mutation). At the end, 20 sub-optimal candidates are identified for the single elastic element. A further selection is then necessary for individuating the best among the proposed solutions. The chosen criterion is to individuate a reasonable compromise among the achievable deflection, the safety margins stress level and the intrinsic stiffness (directly linked to the shape keeping ability). In order to allow a direct comparison of the different performance, involving various parameters and physical meanings, their values are normalised with respect to the respective max. The following expressions are adopted:

- Normalised achieved deflection

$$\overline{\alpha_i} = \frac{\alpha_i}{\max_{i=1..20}(\alpha_i)} \tag{2}$$

Table 2 Materials main properties

Material	Titanium alloy	Stainless steel	Aluminium alloy	SMA (Ni-Ti-Cu)
Young modulus (GPa)	110.	210.	72.	40. (austenite) 23. (martensite)
Poisson modulus	0.32	0.32	0.32	0.32
Density (kg/m^3)	4540.	7850.	2800.	6450.
Stress limit (MPa)	800.	540.	483.	950.
SMA transition T: **Af, As, Ms, Mf (°C)**	-	-	-	85.9, 59.3 35.0, 12.6
Transformation stress vs T rate – C_A, C_M (MPa/°K)	-	-	-	12.0
Specific heat (kJ/kg.°K)	0.540	0.500	0.960	0.837
Max recoverable strain, unloaded, ε_r (%)	-	-	-	8.0

- Normalised deflection, caused by the aerodynamic loads action

$$\overline{\alpha}_{aer,i} = 1 - \frac{\alpha_{aer,i}}{\max_{i=1..20}\left(\alpha_{aer,i}\right)} \tag{3}$$

- Normalised cell material and SMA safety factors

$$\overline{k}_{str,i} = \frac{k_{str,i}}{\max_{i=1..20}\left(k_{str,i}\right)} \tag{4}$$

$$\overline{k}_{SMA,i} = \frac{k_{SMA,i}}{\max_{i=1..20}\left(k_{SMA,i}\right)} \tag{5}$$

- Normalised cell buckling level

$$\overline{F}_{BK,i} = \frac{F_{BK,i}}{\max_{i=1..20}\left(F_{BK,i}\right)} \tag{6}$$

- Normalised cell weight

$$\overline{W_i} = 1 - \frac{W_i}{\max_{i=1..20}(W_i)} \tag{7}$$

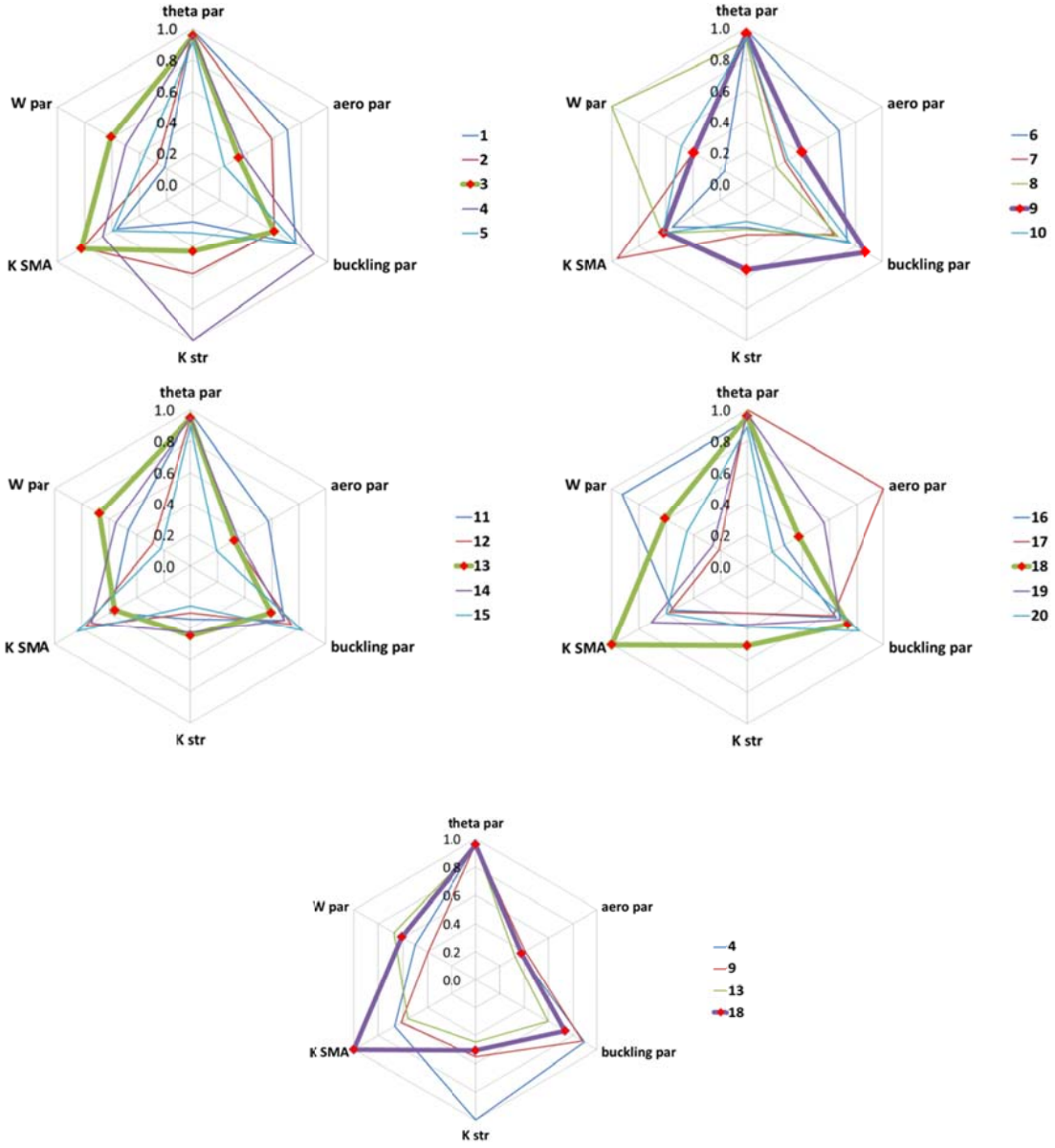

Fig. 5 1st cell; comparison of clusterised 20 solutions (top 4 pictures) and further selection of the best individual (bottom) on the basis of web diagrams representation

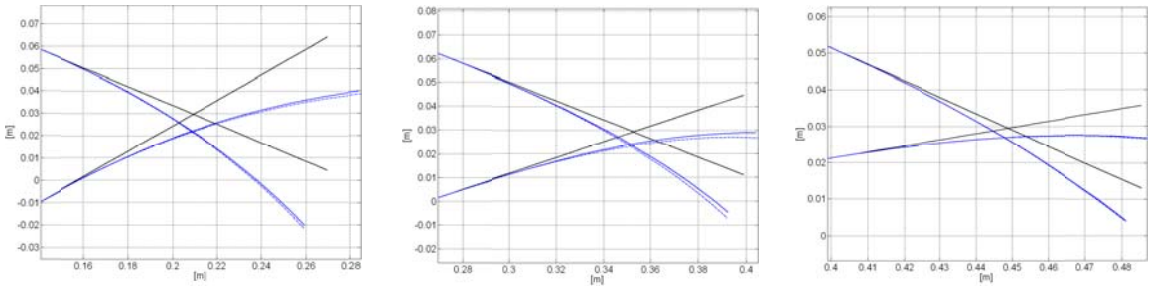

1st cell 2nd cell 3rd cell

Fig. 6 X cells selected configurations: undeformed (black), deformed by SMA action (dashed blue), deformed by combined SMA and aerodynamic action (solid blue)

The different performance levels are then plotted on web diagrams, and a further selection is carried out on the base of the researcher's sensibility and experience. In particular, to provide an operative example of the implemented process, the 20 sub-optimal individuals associated to the 1st cell, were divided into cluster of 5, Fig. 5, top 4 figures. The solutions showing a best balance among the prescribed indexes, were selected (individuals 3, 9, 13 and 18) and further compared in the last plot, Fig. 5, bottom. The individual N.18 was finally selected as the best among the analysed configurations. The same procedure was adopted for the 2nd and the 3rd cells. The resulting 2D layouts are plotted in Fig. 6, where the deformed geometries with and without external loads are reported. It is worth to note that aerodynamics produce an upward rotation that slightly attenuates the SMA action. This means that the system spends the max level of energy in deforming itself more than counteracting the external forces. The main features of the three cells are summarised in Table 3.

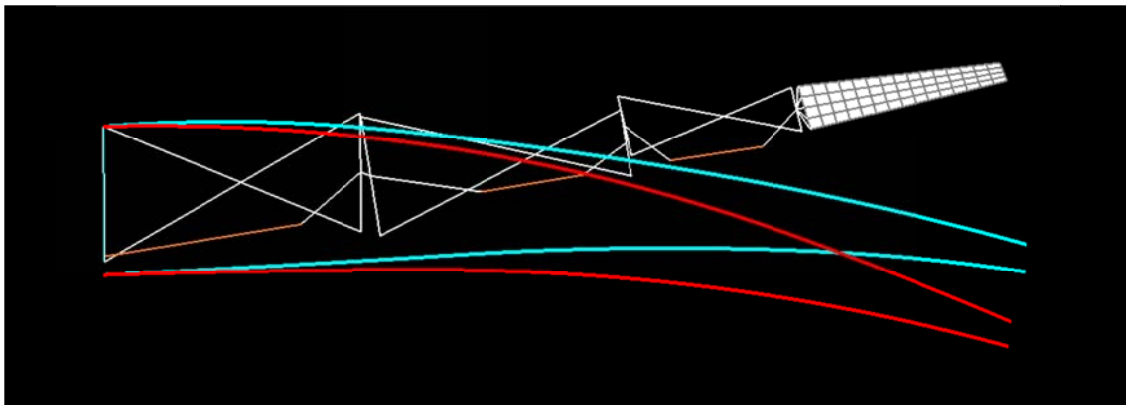

Fig. 7 2D rib: cells (white) & SMA (orange) FE model, undeformed (light blue), and target shape (red)

Table 3 Optimization results

		Cell		
		1st	**2nd**	**3rd**
Cell points	A, abscissa (mm) *	140.5	269.7	399.0
	A, ordinate (mm)	-9.6	1.6	21.1
	B, abscissa (mm) *	269.7	399.0	485.3
	B, ordinate (mm)	4.3	11.0	13.1
	C, abscissa (mm) *	269.7	399.0	485.3
	C, ordinate (mm)	64.1	44.8	35.7
	D, abscissa (mm) *	140.5	269.8	399.0
	D, ordinate (mm)	58.5	62.2	51.9
SMA points	E, abscissa (mm)	140.5	323.0	417.2
	E, ordinate (mm)	-6.8	15.2	9.1
	E, abscissa (mm)	239.2	375.1	464.5
	E, ordinate (mm)	8.4	15.4	5.0
Cell plates	Min/max thickness (mm)	1.0/2.0	1.1/1.5	0.6/1,3
	Min/max width (mm)	4.7/5.9	4.7/5.1	2.3/4.1
SMA features	SMA length (mm)	100.0	52.0	47.0
	SMA cross section (mm^2)	103.0	33.1	69.8
Cell performance	Material		Aluminium	
	Overall cell weight (g)	124.2	58.8	34.2
	Rotation – pre-load (deg):	8.7	4.3	6.2
	Rotation – SMA action (deg):	20.0	20.1	10.4
	Rotation – SMA & aerodyn. loads (deg):	18.8	17.5	10.2

* even though the abscissas of the edges of the cells (A,B,C and D) were not object of optimization, for sake of completeness were reported

Having assessed the cells outline, a 2D FE model of a complete rib is realized, Fig. 7, Table 4. Non linear static investigations permit estimating the behaviour of the combined cells system under pre-load and when activated. Because the selected solutions overperformed the requirements, an intermediate configuration is also considered, corresponding to the attainment of the reference target morphed shape, Fig. 7. The pre-loads system ensures the achievement of the initial shape under the combined action of the external (producing an upward deflection) and inner forces

(moving back the rib to its neutral position). The activation of the SMA elements then deflects the structure up to the target morphed shape, Fig. 8.

The FE analysis enables to estimate the expected trailing edge vertical displacements and related stress levels within the cell materials and inside the SMA for each of the considered conditions (pre-load, partial and full SMA activation). All these data are reported in Table 5, together with the safety factors and required temperatures for driving the shape memory alloys actuators. The related necessary energy level is estimated by multiplying the SMA mass by its specific heat and the difference between the required and the environmental temperature (25°C – SMA material is designed to be inert at standard T_{room}).

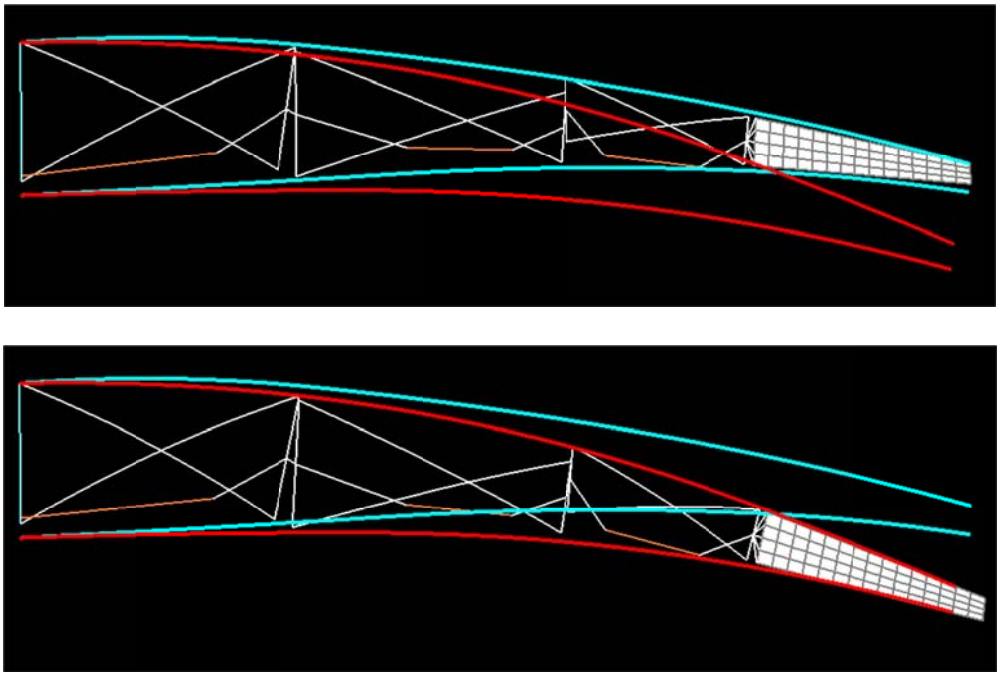

Fig. 8 Flap initial (top) and target (bottom) morphed shapes fitting

Table 4 2D rib FE model data

Number of elements	241
Number of nodes	251
Type of elements	• beams for the cells and the SMA, • plates for the rigid trailing edge • rigid links for the connections of the cells
Cells material	Aluminium alloy (Table 2)

Table 5 2D rib performance

Feature	Pre-load	Intermediate	Fully activated
Max vertical disp.(mm) *	92.2	137.6	336.4
Max stress within the cells (MPa)	61.6	90.2	249.9
Max stress within SMA (MPa)	150.0	224.7	823.0
Overall safety factor **	6.3	4.2	1.2
Activation temperatures (°C) ***	-	85.4	128.4
Energy (kJ) ****	-	4.1	6.4

* with respect to the deformed configuration, following aerodynamics action
** min between SMA elements and cells safety factors
*** max temperature among the three cells
**** referring to a 25°C environmental temperature

5. Advanced design

After the conceptual and optimization design phase, the flap advanced sizing is faced. This task is aimed at producing preliminary drawings of the prototype, having taken into account issues linked to the device manufacturing and its practical use. A CAD model of the flap is shown in Fig. 9, where the internal actuation architecture can be seen. A 1 m span, 3-bay flap is considered. Both the upward and downward plates (AC and BD segments, Fig. 4) of each cell is split into two further equal elements, distributed span-wise, Fig. 10. This architecture guarantees the absence of any interference during motion.

The model takes into account assembly operations. For instance, to assure the due SMA pre-load, each elastic cell is first bent downward and integrated with the SMA elements. The elastic reaction stretches the shape memory alloy segments, attaining the required preload at the desired reference configuration. It is worth to note that if the cells are mounted in this condition, an additional curvature is introduced to the clean flap configuration. To compensate this effect, each cell has to be mounted with an opposite pitch angle. Furthermore, the installation should be tuneable, in order to compensate possible assembly errors or material characteristics variation. A dedicated mounting solution is thus devised and sketched in Fig. 10. The cells are connected each others through hinges; screw-nut elements allow approaching and spacing the points G and H, so to regulate their relative angle and assure a suitable blockage around the pivots. SMA elements are connected to the structure by the modular bushes illustrated in Fig. 11. The bushes are mounted within the cells (details in Fig. 10) and are insulated from the other metallic parts through nylon rings. This arrangement assures a safe heating of the SMA actuators by Joule effect.

A complete FE model of the flap system is shown in Fig. 12. Shell elements model the cells and their connections; SMA components are modelled through beam elements, connected to the cells by rigid bars. The pinned constraint is simulated by releasing the rib in-plane rotations at the SMA edges, Fig. 12. As for the 2D model, the shape memory alloy action is simulated by assigning a dummy expansion coefficient to the material. Beam elements are also used for modelling the screw-nut systems, while rigid connections, enabling only in-plane rotations, are used to simulate the cells hinges. Three spars connected spanwise the respective cells, each bolted onto the cells boundaries, Fig 12. Three shape, passive ribs are added at intermediate stations, to further stiffening the skin under the external pressure loads. A summary of the main features of the flap model is reported in Table 6. The total weight results into 5.69 kg, while the centre of gravity of the architecture is located 325.2 mm from the flap leading edge.

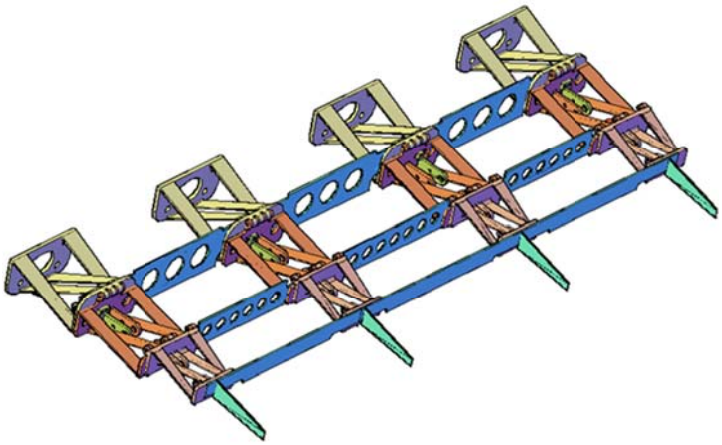

Fig. 9 CAD model of the flap morphing architecture

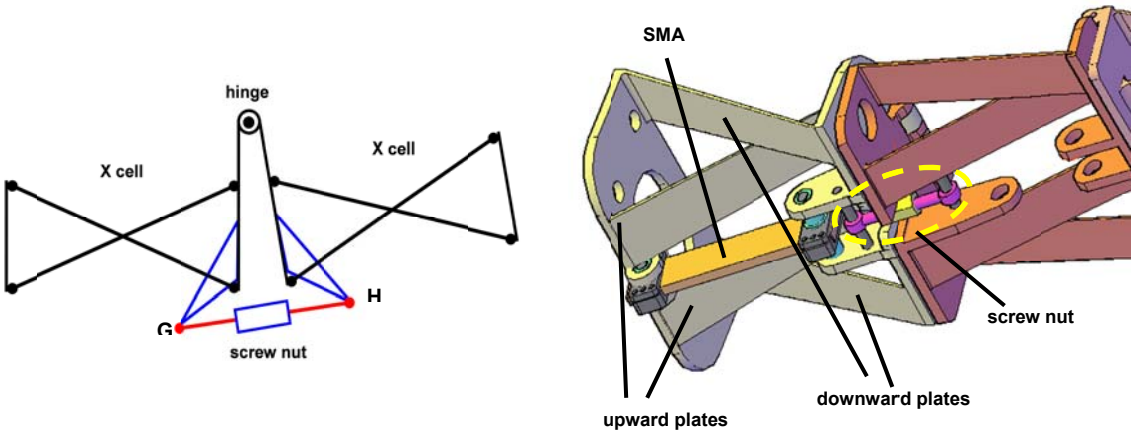

Fig. 10 Scheme of the screw nut system (left); CAD implementation (right)

Table 6 Flap main features

Component / subcomponent	**Weight (kg)**	**Quantity**	**Total weight (kg)**
1st cell	0,28	4	1,13
SMA 1st cell	0,07	4	0,26
2nd cell	0,19	4	0,74
SMA 2nd cell	0,01	4	0,04
3rd cell	0,10	4	0,39
SMA 3rd cell	0,02	4	0,08
rib final segment	0,00	4	0,02
active rib	**0,67**	4	**2,66**
intermediate rib	**0,02**	3	**0,07**
1st spar	0,33	1	0,33
2nd spar	0,19	1	0,19
3rd spar	0,06	1	0,06
All the spars	**0,57**	1	**0,57**
Stiffener	**0,01**	9	**0,11**
Skin	**2,27**	1	**2,27**
		Total	**5,69**

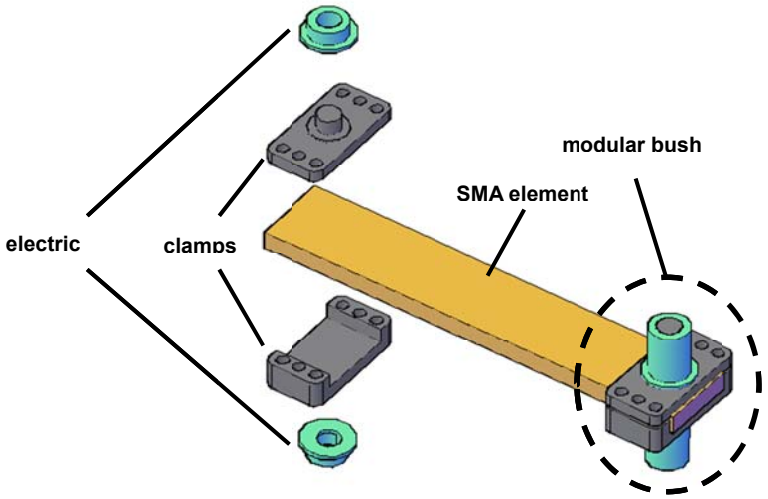

Fig. 11 Modular bushes for SMA connection

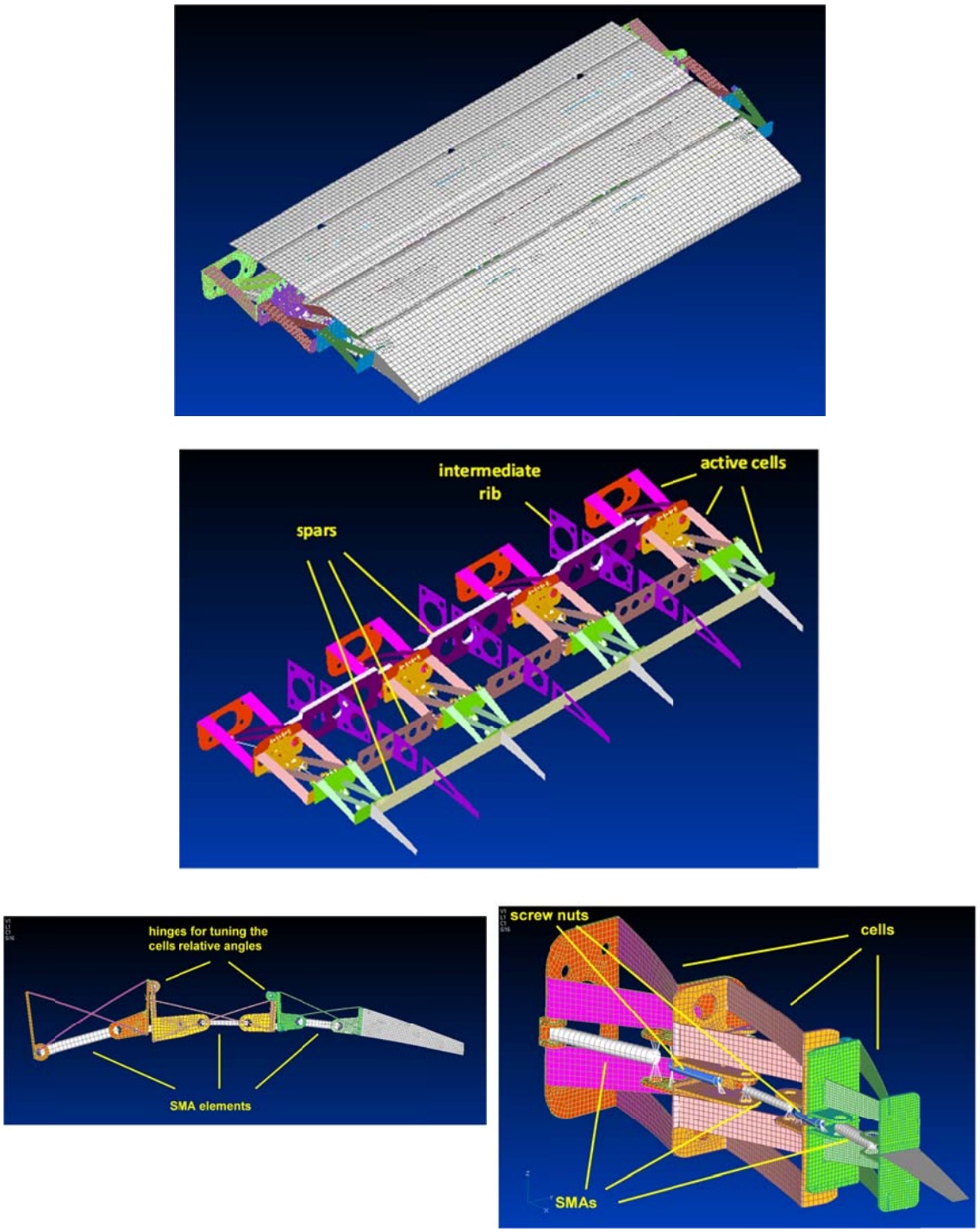

Fig. 12 Flap FE model: complete (top); internal structure (middle); rib details (bottom, left/right)

6. Numerical results

Pre-load, intermediate and full-activated configurations (corresponding to clean, intermediate and max rotation deformed shapes, respectively) are each characterised through devoted static analyses. The aim of the simulations is to appreciate the morphing ability of the proposed system and to verify the achieved stress levels. A short summary of the results is reported in Table 7.

The aerodynamic loads are applied as a 2D distributed pressure on the skin, according to the profile illustrated in Fig. 2. Their effect on the flap shape is shown to be practically negligible with respect to the other forces acting on the structural system (related tip rotation and displacement resulted -0.386 deg and 4.18 mm, respectively). An ever more negligible effect was observed for the pre-load configuration, because of the reduced magnitude of the aerodynamic loads at this attitude.

The arising stress field (max value estimated at 159.7 MPa) affected prevalently the skin, as shown by the contour map, reported in Fig. 13. A different situation occurs when the inner actuators command the downward movement of the adaptive flap, when the most solicited components are cell plates. This situation is also illustrated in Fig. 13. The max stress level within the structure at 251.3 MPa, well below the material stress limit (483 MPa), with a safety factor of about 2.

The normal mode analysis, where the effects of the SMA induced stress are taken into account by the differential stiffness matrix, does not show appreciable effects on the eigen-frequencies of the activated and non-activated configurations. The first 3 modal shapes are displayed in Fig. 14. The 1st and the 2nd modes correspond to a natural morphed shape, coherent with the set-up actuation system, while the 3rd mode regards the span direction. Buckling analysis verifies the simultaneous action of the external (aerodynamic) and internal (actuation) loads does not produce instabilities.

Table 8 summarises the obtained results, enough robust for each of the investigated scenarios (isolated and combined loads). The reported numbers mean the load multipliers to have instability. A negative sign denotes the sense of the load that would cause buckling is opposite, then not applicable to the conventional device action. In spite the former and this analyses are not in principle correlated, the safety factor is estimated once again to about 2.

Table 7 3D FEM results

	Aerodynamic loads	**Intermediate config.**	**Fully activated config.**
TE vertical displ. (mm) *	-4.18	92,7	227,8
Global rotation (deg) **	-0.386	8.5	15.2
Max stress within the structure (MPa) ***	159.7	154,2	251,3

* with respect to the pre-load condition
** slope of the straight line connecting the flap root to the TE position
*** for the stress within the SMA elements, refer to data of Table 5

Table 8 Buckling eigenvalues

Aerodynamic loads	Full activation loads	Combined loads
-2.0	3.48	1.9

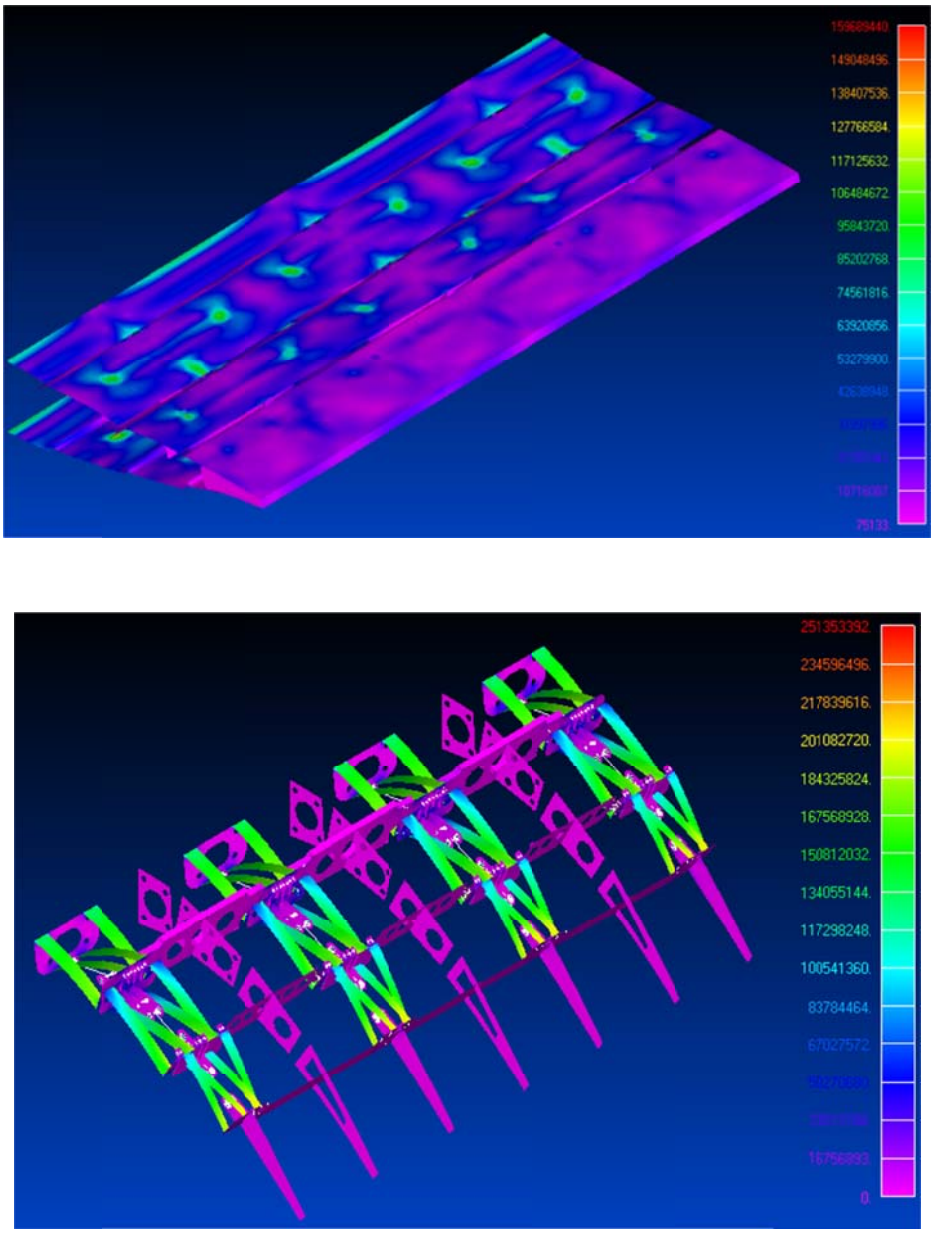

Fig. 13 Stress distribution due to the aerodynamic (top) and combined load system (bottom)

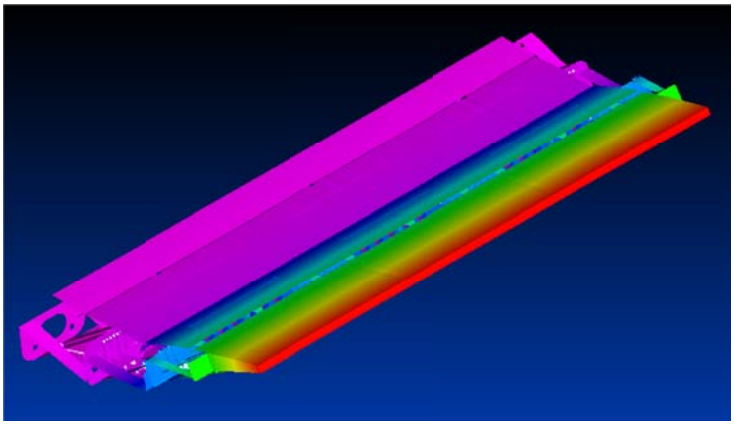

1st mode: 13.7 Hz

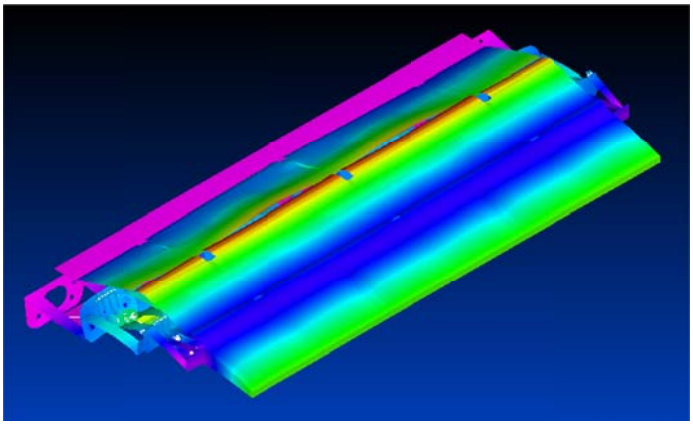

2nd mode: 70.0 Hz

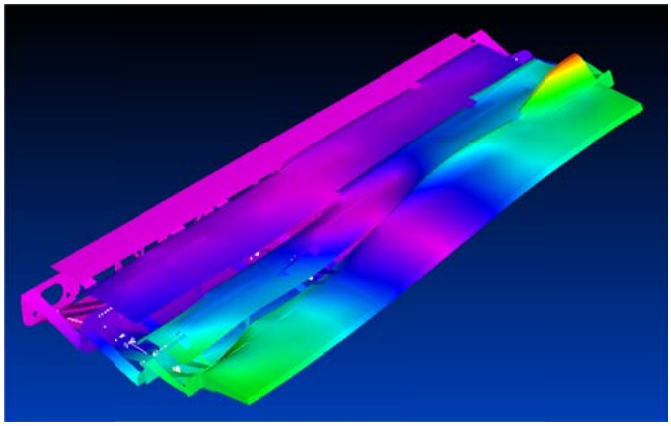

3rd mode: 85.7 Hz

Fig. 14 First 3 modal shapes of the flap

7. Conclusions

In this paper, a novel procedure combining preliminary and advanced design of a morphing flap aimed at augmenting hyperlift generation is presented. In order to achieve the desired morphing capabilities, the original flap ribs are segmented and joint by elastic elements, passive (cells) and active (SMA-based actuators). Both these elements have structural capabilities. Shape memory elements contraction forces the respective cell to bend and produce a consequent variation of the flap camber. The peculiar geometric configuration of the cells, made of non-interfering crossing plates, confers the system a wide flexibility and ability in bearing loads.

At first, the conceptual architecture design is developed. The range of the most important design parameters, like the cross section and the orientation of the elastic plates, the cross section of the SMA actuators and their connection (hinges) to the reference structure, were set. An optimisation code, based on the use of genetic algorithm, exploited a simple FE model of the elementary cell, identifying sub-optimal configurations. The optimisation target was to maximise the attained deflection within the constraints of the material and stability limits (max stress and buckling loads). Further parameters do then allow selecting the best architecture as a compromise of performance and weight penalty, stiffness characteristics (ability to maintain a certain shape under the action of the external loads) and so on. The process is carried out for all the three active cells, undergoing a different load system.

The advanced design of the flap is then performed. In the reported case, a 3-bay constant-chord flap is outlined, with the aim of verifying the capability of 3D system to carry out both internal and external loads, within its due physical (max stress value) and geometrical (buckling loads) limitations. Important manufacturing aspects are considered like the pre-load tuning; the electrical insulation of the SMA components; the active ribs span-wise connection; the presence of a skin (having the main role to properly distribute the aerodynamic pressure over the structural elements); the further stabilization of the structural system (and particularly the skin) through the insertion of additional passive (shape) ribs.

The CAD drawings are then used to produce a complete FE model of the flap. Static analyses are carried out to characterise the flap behaviour in terms of effective capability of achieving the specified shape and bearing the arising stress field. The effects related to the aerodynamic loads are shown to be negligible with respect to the other concurring forces, with the exception of the skin, where levels are relevant. The normal mode analysis verifies as well that the external and internal force action (and consequent differential stiffness matrix and differential geometrical configuration do not relevantly affect the structural system eigenvalues and eigenvectors. Buckling analysis finally confirms the good stability levels of the proposed device.

Obtained results push an interest for further investigations about the herein presented architecture. The realisation of an experimental demonstrator should be pursued in order to verify its static and dynamic behaviour in lab, with the perspective of preliminary wind tunnel experiments. Manufacturing issues, interference aspects, power feeding concerns and many other aspects are relevant topics to be addressed. Also, the aerodynamic behaviour of the segmented structure is a point worth to be investigated, both at level of aerodynamic performance and noise generation. SMA installation questions, aging and fatigue response of the active elements, pre-load tuning and adaptive systems aimed at self-balancing the shape during operations, are other themes worth to be faced and deepened. Finally, a suitable shape control system should be developed, taking into account the peculiarities of the structural elements and the selected actuators; in this sense, the logic architectures proposed by (Langbein and Welp 2009, Dimino and Concilio 2013)

seem good candidates to these purposes.

Acknowledgments

Part of this research was funded by the Clean Sky Joint Undertaking under project GAM-GRA (Grant Agreement for Member – Green Regional Aircraft), related to activities performed within the ITD (Integrated Technology Demonstrator) Green Aircraft.

References

Advisory Council for Aviation Research and Innovation in Europe, ACARE http://www.acare4europe.org/sites/acare4europe.org/files/attachment/SRIA%20Volume%201.pdf

Ameduri, S., Brindisi, A., Tiseo, B., Concilio A. and Pecora, R. (2013), "Optimization and integration of shape memory alloy (SMA)-based elastic actuators within a morphing flap architecture", *J. Intell. Mat. Syst. Str.*, **23**(4) 381-396.

Carruthers, A.C., Walker, S.M., Thomas, A.L.R. and Taylor, G.K. (2010), "Aerodynamics of aerofoil sections measured on a free-flying bird", *J. Aerospace Eng.*, **224**(8), 855-864.

Concilio, A. and Ameduri, S. (2013), "Influence of structural architecture on linear shape memory alloy actuator performance and morphing system layout optimization", *J. Intell. Mat. Syst. Str.*, 1045389X13517306, first published on-line, December 31, 2013.

Daniele, E., De Fenza, A. and Della Vecchia, P. (2012), "Conceptual adaptive wing-tip design for pollution reductions", *J. Intell. Mat. Syst. Str.*, **23**(11), 1197-1212.

Dimino, I. and Concilio, A. (2013), "An adaptive control system for wing TE shape control", *Proceedings of the SPIE International Conference on Smart Structures*, San Diego, California, March.

Grigorie, T.L., Popov, A.V., Botez, R.M., Mamou, M. and Mébarki, Y. (2011a), "On-off and proportional-integral controller for a morphing wing. part 1: actuation mechanism and control design", *J. Aerospace Eng*., **226**(2), 131-145.

Grigorie, T.L., Popov, A.V., Botez, R.M., Mamou, M. and Mébarki, Y. (2011b), "On–off and proportional–integral controller for a morphing wing. part 2: control validation – numerical simulations and experimental tests", *J. Aerospace Eng.*, **226**(2), 146-162.

Langbein, S. and Welp, E.G. (2009), "One-module actuators based on partial activation of shape memory components", *J. Mater. Eng.Perform.*, **18**(5-6), 711-716.

Lesieutre, G.A., Browne, J.A. and Frecker, M.I. (2011), "Scaling of performance, weight, and actuation of a 2-d compliant cellular frame structure for a morphing wing", *J. Intell. Mat. Syst. Str.*, **22**(10), 979-986.

Maheri, A. and Isikveren, A.T. (2011), "Design of a single-dof kinematic chain using hybrid GA-pattern search and sequential GA", *J. Mech. Eng. Sci.*, **226**(6), 1634-1643.

Mcknight, G., Doty, R., Keefe, A., Herrera, G. and Henry, C. (2010), "Segmented reinforcement variable stiffness materials for reconfigurable surfaces", *J. Intell. Mat. Syst. Str.*, **21**(17), 1783-1793.

Nadar, A., Khan, R., Jagnade, P., Limje, P., Bhusari, N. and Singh, K. (2013), "Design and analysis of multi-section variable camber wing", *Int. J. Mech. Eng. Robot.*, **1**(1), 122-128.

Olympio, K.R. and Gandhi, F. (2010), "Flexible skins for morphing aircraft using cellular honeycomb cores", *J. Intell. Mat. Syst. Str.*, **21**(17), 1719-1735.

Pecora, R., Amoroso, F., Magnifico, M. and Concilio, A. (2013), "Design and experimental validation of a morphing wing flap device", *Proceedings of the 6th ECCOMAS Conference on Smart Structures and Materials*, SMART2013, Turin, Italy, June.

Smart Intelligent Aircraft Structures, SARISTU, http://www.saristu.eu

Stanewsky, E. (2001), "Adaptive wing and flow control technology", *Prog. Aerosp. Sci*., **37**(7), 583-667.

Tomassetti, G., Ameduri, S. and Carozza, A. (2011), "Innovative streamline-flow preserving actuation strategies for wing airfoil nose", *Int. J. Struct. Integrity*, **2**(4), 437- 457.
Wildschek, A., Havar, T. and Plötner, K. (2010), "An all-composite, all-electric, morphing trailing edge device for flight control on a blended-wing-body airliner", *J. Aerospace Eng.*, **224**(1), 1-9.
Zhao, J.S., Ye, L., Chu, F. and Dai, J.S. (2012),"Synthesis and static analysis of the deployable frame for a morphing wing", *J. Mech. Eng. Sci.*, **227**(3), 565-579.

CC

Acronyms and symbols

A	cross section area
A,B,C,D	"X cell" plates edges
ACARE	Advisory Council for Aeronautics Research in Europe
A_f	austenite finish temperature without mechanical loads
A_s	austenite start temperature without mechanical loads
c	chord
CAD	Computer Aided Design
E	Young modulus
E, F	SMA edges
F	force
FE	Finite Element
$F_{BK\,i}$	minimum force producing instability (i^{th} individual)
$\bar{F}_{BK}$	normalised minimum force producing instability
G, H	screw nut edges
$k_{str\,i}$	cell material safety factor (i^{th} individual)
$\bar{k}_{str}$	normalised cell material safety factor
$k_{SMA\,i}$	SMA material element safety factor (i^{th} individual)
$\bar{k}_{SMA}$	SMA material normalised safety factor
L/D	lift – drag ratio
M_f	martensite finish temperature without mechanical loads
M_s	martensite start temperature without mechanical loads
MAC	Mean Aerodynamic Chord
$_{pl}$	subscript referring to the pre-load condition
s	SMA axial displacement (abscissa of the graph of Fig. 3)
$_{SMA}$	subscript referring to SMA material
T	thermal load
T_{room}	environnmental temperature (25°C)
$_{wk}$	subscript referring to fully activated working condition
x	dimensionless abscissa
z	dimensionless ordinate
W_i	weight (i^{th} individual)
$\bar{W}$	normalised weight
α_T	thermal coefficient
α_i	SMA induced deflection (i^{th} individual)
$\bar{\alpha}$	normalised SMA induced deflection
$\alpha_{aer\,i}$	induced deflection due to external aerodynamic loads (i^{th} individual)
$\bar{\alpha}_{aer}$	normalised induced deflection due to the external aerodynamic loads
ε	strain
ε_{max}	max SMA recoverable strain, fully activated work condition
ε_r	recoverable strain without loads